Research Performance Progress Report

Grant Proposal:
DE-SC0008823 (referred to as DE-FG52-09NA29548)

Project Title:
Diverging Supernova Explosion Experiments on NIF

PI:
Tomasz Plewa, Dr., tplewa@fsu.edu, (850) 459-0997 (cell)

Submission Date:
05/03/2013 (original), 07/22/2013 (this version)

Recipient Organization:
Florida State University
874 Traditions Way
Tallahassee, FL 32306-0001

Project/Grant Period:
start: 08/01/2012, end: 07/31/2015 (no cost 07/31/2016)

Reporting Period End Date:
07/31/2016

Report Term or Frequency:
final

Abstract

The aim of this project was to design a series of blast-wave driven Rayleigh-Taylor (RT) experiments on the National Ignition Facility (NIF). The experiments of this kind are relevant to mixing in core-collapse supernovae (ccSNe) and have the potential to address previously unanswered questions in high-energy density physics (HEDP) and astrophysics. The unmatched laser power of the NIF laser offers a unique chance to observe and study “new physics” like the mass extensions observed in HEDP RT experiments performed on the Omega laser [1], which might be linked to self-generated magnetic fields [2] and so far could not be reproduced by numerical simulations. Moreover, NIF is currently the only facility that offers the possibility to execute a diverging RT experiment, which would allow to observe processes such as inter-shell penetration via turbulent mixing and shock-proximity effects (distortion of the shock by RT spikes).

1. Accomplishments

1.1 Scope of the project

In the course of this project, we performed numerical simulations using the adaptive-mesh radiation magnetohydrodynamics (MHD) codes CRASH, FLASH, and Proteus to guide the experiment design. The codes include extensive HEDP capabilities, like 3-temperature hydrodynamics, multigroup radiation transport, tabulated EOS, laser ray tracing and multi-material treatment. Using different codes at the same time is helpful in improving computational machinery. We have implemented the extended MHD formulation according to Braginskii [3] in our version of the FLASH code [4], Proteus, which puts us into a position to study the influence of magnetic fields generated via the Biermann battery effect on the RT morphology.

Our strategy towards fielding a diverging RT experiment on NIF was to perform a planar experiment first in order to develop the drive and diagnostics platforms. As the next step, we were to consider experiments with a non-planar (but forward-propagating) shock wave, and finally, experiments with a diverging shock. The planar design was finished [5]. However, the promised NIF shots never materialized leaving our project in a state of limbo. Nevertheless, we continued the design study by enriching the planar RTI design by new physics (magnetic fields), as reported in [9], and considering closely related Kelvin-Helmholtz instability problem in the HEDP setting (in a doctoral project).

In what follows, we first summarize the results obtained in the planar design study (Sec. 1.2), accomplishments in Year 3 and during the no-cost extension period (Sect. 1.3), before we move on to discuss our plans for the future (Sec. 1.4).

1.2 Planar target design study

Target setup We used the CRASH code to simulate the design of the planar target. The target is two-layered, with the heavy material being copper and the light material plastic. Three NIF cones are used to illuminate the target, with the fourth cone being reserved to generate diagnostic x-ray photons. We used analytic estimates together with numerical simulations in order to optimize the laser drive and the target parameters for optimal diagnostic results. Fig. 1 shows a sketch of the proposed setup.

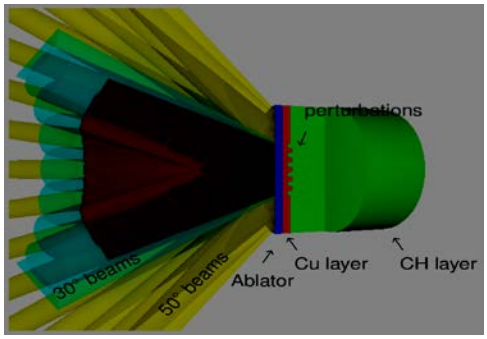

Fig. 1: Sketch of the experimental setup.

Synthetic radiographs We have developed a radiographic model that accounts for the fact that outside the "perturbed region" (where the Cu/CH interface is flat, see Fig. 1), copper structures will "wrap around" and (due to the very high opacity of copper) pose the danger to reduce the signal in the region of interest. Our radiographic model includes photon shot noise (the dominant noise source) and motion blur (blurring of radiographs due to target motion). We are able to show that the experiment can be diagnosed using currently available point-projection x-ray radiography capabilities on NIF. We find that using zinc as the backlighter material gives the best results and that using higher drive energies lead to better radiographic contrast. See Fig. 2 for example radiographs.

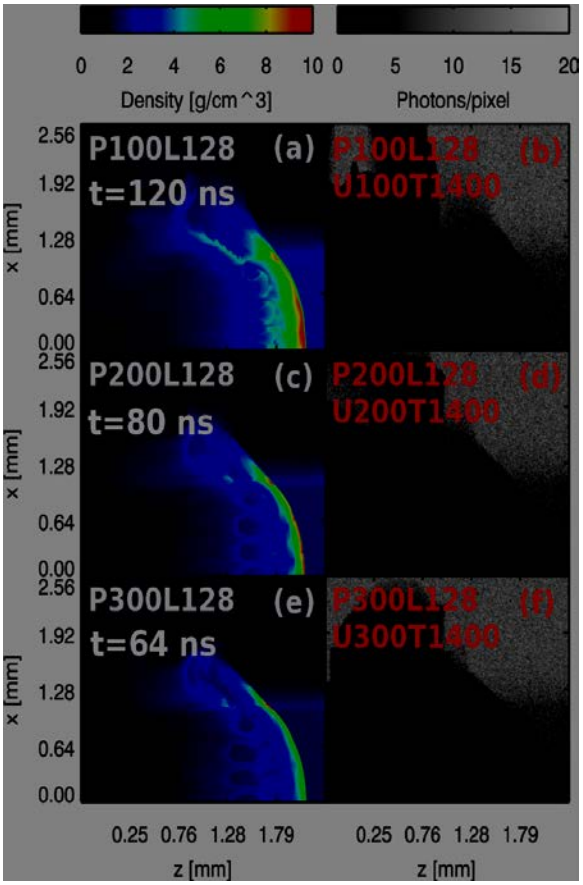

Fig. 2: Density plots (left) and simulated radiographs (right) for different drive energies (top: 100 kJ, middle: 200 kJ, bottom: 300 kJ).

Sensitivity to numerical diffusion We conducted a rigorous study on the dependence of the simulation results on the effective numerical resolution, finding that the width of the mix layer (the region where copper and plastic are mixed) is converged at a resolution of 1 micron.

Sensitivity to the drive energy We explored drive energies in the range between 80-300 kJ and find that higher drive energies lead to better radiographic contrast and a deeper spike penetration. Since the time delay between drive and diagnostic beams is also shorter at higher energies, using 300 kJ of drive energy is highly favored.

Target construction uncertainties We used high-resolution simulations to study the influence of small-scale perturbations (that might be introduced during the process of target fabrication) on the RT morphology. We were able to show that for perturbations smaller than 1 micron (which is significantly greater than the size of typical fabrication errors) the effect is small.

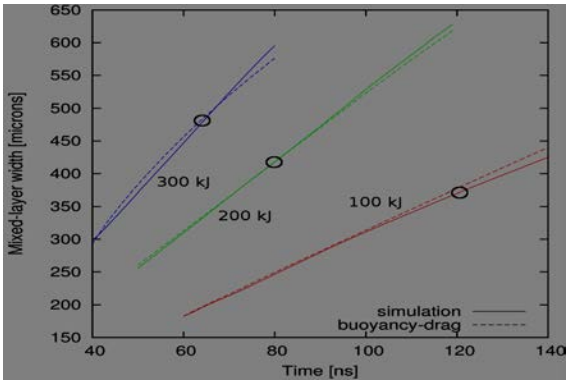

Fig. 3: Mix layer width in simulations vs. prediction of buoyancy-drag model.

Buoyancy-drag model On the basis of previous work [6,7], we developed a buoyancy-drag model to describe the evolution of the mix layer during the nonlinear stage of the RT instability [5]. Our model predicts the evolution of the mix layer using only data from a 1D simulation. We find excellent agreement between our simulation results and the buoyancy-drag model (Fig. 3) for the whole range of drive energies considered. This verifies that the mixing observed in the simulations is indeed due to the RT instability.

1.3 Accomplishments in Year 3 and during the no-cost extension period

1.3.1 Influence of self-generated magnetic fields on RT morphology Magnetic fields generated by the Biermann battery effect are possibly important both in ccSNe [8] and HEDP experiments [2]. We used our version of the FLASH code, which includes the extended MHD formulation according to Braginskii [4], to study the influence of self-generated magnetic fields [2] on the RT morphology in HEDP experiments. We have already studied self-generated magnetic fields in gravity-induced RT instability [4].

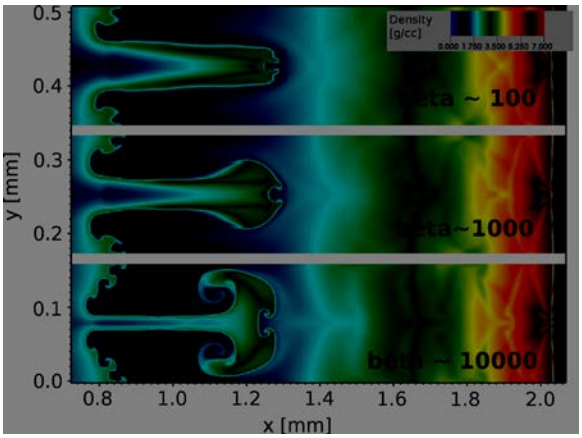

Fig. 4: Spike morphology in blast-wave RT simulations with preimposed longitudinal magnetic field of different strength (beta=final plasma beta).

Preliminary simulations of a blast-wave driven RT systems with pre-imposed magnetic fields show dramatic morphology changes already for very weak fields (Fig. 4), as we reported in the recently published paper [9], with structures resembling those found in the experiments performed by Kuranz et al. [1].

1.3.2 The Braginskii model implementation

Anisotropic Conductivity Implementation and Verification We have implemented in the code an explicit (and now, after further work, an implicit solver for the anisotropic thermal conductivity given in Braginskii as

$$\vec{q} = \left(-\kappa_{\parallel} B_i B_j - \kappa_{\perp}\left(\delta_{i,j} - B_i B_j\right) - \kappa_{\wedge}\epsilon_{jki} b_k\right)$$

This conductivity is implemented by explicitly modifying the heat fluxes along cell boundaries with the effect of the magnetic field strength on thermal conductivity taken into account. Because this anisotropy manifests itself in temperature (as opposed to say viscosity), implementation of a verification test problem for this model was relatively straightforward. We used the Stone and Parrish test problem for this purpose, where a strictly solenoidal magnetic field was initialized around some center point in an isothermal

medium. We the initialize a small subportion of a toroidal ring of higher temperature and let the system evolve (with the solenoidal magnetic field being imposed in time). This is depicted in Figure 5.

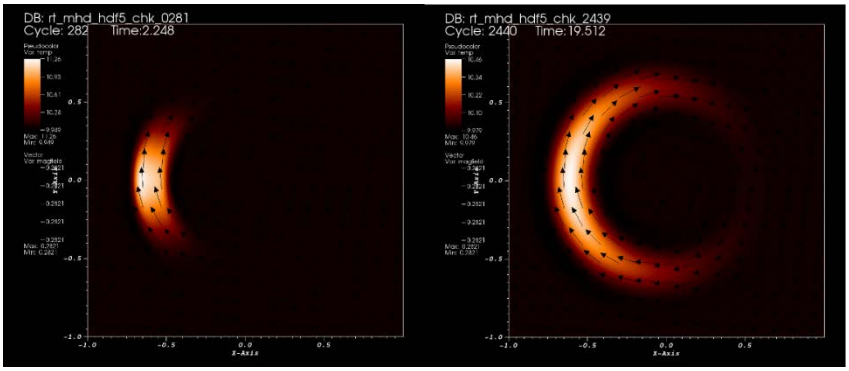

Figure 5: Evolution of the Parrish-Stone test problem for anisotropic conductivity

As is demonstrated, the overwhelming amount of the thermal energy initialized within the annulus remained within the annulus through evolution in time, as one would expect due to magnetic field driven conductive anisotropy. To further verify our code, we model the above configuration on various grid sizes and looked at the residual as a function of the grid size.

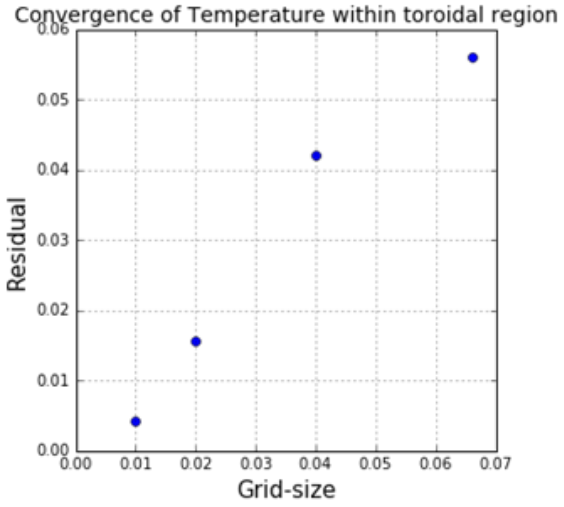

Figure 6: Convergence of the residual between the simulated and exact solutions for the Parrish-Stone Annulus Problem on various grid sizes.

Method of Manufactured Solutions for Compressible Plasmas As in the proceeding section regarding conductivity, we have implemented the Braginskii model for anisotropic viscosity due to magnetic fields in our Proteus code. While the viscous stress tensor in isotropic is described by a single viscosity coefficient and a single strain-rate tensor of the form

$$\pi_{i,j} = \eta_0 W_{i,j}$$

The introduction of magnetic field driven viscous anisotropy in three dimensions necessitates a linear combination of 5 viscous coefficients (from microphysics) and 5 strain rate tensors, themselves functions of the unmodified strain rate tensor above, this being given as

$$\pi_{i,j} = -\eta_0 W^0_{i,j} - \eta_1 W^1_{i,j} - \eta_2 W^2_{i,j} + \eta_3 W^3_{i,j} + \eta_4 W^4_{i,j}$$

These strain-rate tensors are themselves functions of the isotropic strain rate tensor and various magnetic field components, with the first and simplest of these being given as

$$W^0_{i,j} = \frac{3}{2}\left(B_i B_j - \frac{1}{3}\delta_{i,j}\right)\left(B_k B_l - \frac{1}{3}\delta_{k,l}\right) W_{k,l}$$

Given the much more complicated functional dependence on the magnetic field of viscosity, and owing to the nonlinear nature of the Navier-Stokes equations in terms of velocity (of which viscosity is a function), the creation of an intuitive test setup in order to verify correct implementation of the model is not possible. Instead, we were forced to devote our energy into the creation of a comprehensive framework for testing problems via the method of manufactured solutions, and have demonstrated its accuracy in verifying the following dynamical systems.

- Pure Inviscid Advection (Moving Gaussian Pulse Problem):

$$\frac{\partial \vec{u}}{\partial t} + (\vec{u} \cdot \nabla)\vec{u} = 0$$

- Pure Pressure-driven Expansion (Expanding Gaussian Pulse Problem):

$$\frac{\partial \vec{u}}{\partial t} + \frac{\nabla p}{\rho} = 0$$

- Full Euler-equation evolution (Isentropic Vortex Problem, grid convergence given in Figure 6):

$$\frac{\partial \vec{u}}{\partial t} + (\vec{u} \cdot \nabla)\vec{u} + \frac{\nabla p}{\rho} = 0$$

We completed a verification of our isotropic viscosity module via a method of a manufactured solution approach to the Navier-Stokes momentum equation, and once that is completed, we can move on to final verification of our implementation of Braginskii anisotropic viscosity.

1.3.3 Anisotropic Diffusion with Multigrid

Electron heat conduction in magnetized plasmas gives rise to thermal diffusion equations of the form

$$\frac{\partial T}{\partial t} - \beta(\boldsymbol{x}, T)\nabla \cdot [\boldsymbol{D}(\boldsymbol{x}, T) \cdot \nabla T] = S(\boldsymbol{x}, T),$$

where β is related to local plasma conditions, T is the electron temperature, and $\boldsymbol{D}$ is the diffusion coefficient tensor. For certain conditions, $\boldsymbol{D}$ is anisotropic, spatially dependent, and may introduce non-linearity through dependence upon T.

Additionally, the diffusion process may operate on much shorter timescales than other physical processes, such as hydrodynamics [4,5]. As such, the heat conduction should be evolved implicitly to enable evolution of the complete system to relevant times. In the following we present an overview of our work toward implementing implicit, anisotropic diffusion into our block-AMR hydrocode Proteus.

Temporal Discretization

$$T^{n+1} - \Theta \Delta t \beta^{n+1} \nabla \cdot (\boldsymbol{D}^{n+1} \cdot \nabla T^{n+1}) - \Theta \Delta t S^{n+1} = T^n + (1-\Theta)\Delta t \beta^n \nabla \cdot (\boldsymbol{D}^n \cdot \nabla T^n) + (1-\Theta)\Delta t S^n$$

We discretize the diffusion equation in time using the general Θ-method. This formulation encompasses explicit forward Euler ($\Theta = 0, O(\Delta t)$), implicit Crank-Nicolson ($\Theta = 0.5, O(\Delta t^2)$), and fully implicit backward Euler ($\Theta = 1, O(\Delta t)$). While Crank-Nicolson is second order in time, it is prone to oscillatory (albeit stable) behavior when the numerical solution includes steep numerical gradients. However, backward Euler may add large numerical diffusion to the solution in the limit of large time steps (Courant factor $\gg 1$) due to its first order approximation.

Spatial Discretization Here we consider the spatial discretization of the diffusion system in Cartesian coordinates. The diffusion operator may be expanded into components such

that

$$\nabla \cdot [\boldsymbol{D} \cdot \nabla T] = \sum_{\alpha=1}^{d} \frac{\partial}{\partial \xi_\alpha}\left(D^{\alpha\alpha}\frac{\partial T}{\partial \xi_\alpha}\right) + \sum_{\beta=1}^{d}\sum_{\alpha=1,\alpha\neq\beta}^{d} \frac{\partial}{\partial \xi_\beta}\left(D^{\alpha\beta}\frac{\partial T}{\partial \xi_\alpha}\right)$$

where $\xi_1 \equiv x$, $\xi_2 \equiv y$, $\xi_3 \equiv z$, and d is the dimensionality of the problem. The first summation represents the "normal" transport of *T*, while the second summation incorporates the "transverse" transport of T. Note that for isotropic diffusion problems ($\boldsymbol{D} = D\boldsymbol{I}$) the transverse components vanish and only the normal components remain. The indices for the tensor elements is provided by

$$\boldsymbol{D} = \begin{bmatrix} D^{11} & D^{21} & D^{31} \\ D^{12} & D^{22} & D^{32} \\ D^{13} & D^{23} & D^{33} \end{bmatrix}$$

We approximate the normal components as the unmodified flux through the axis-aligned interfaces of a cell specified by indices (i, j, k) on a locally uniform grid. The contribution for faces partitioning the *x*-axis is given by

$$\frac{\partial}{\partial x}\left(D^{11}\frac{\partial T}{\partial x}\right) \approx -\frac{D^{11}_{i+\frac{1}{2},j,k} + D^{11}_{i-\frac{1}{2},j,k}}{\Delta x^2} T_{i,j,k} + \frac{D^{11}_{i+\frac{1}{2},j,k}}{\Delta x^2} T_{i+1,j,k} + \frac{D^{11}_{i-\frac{1}{2},j,k}}{\Delta x^2} T_{i-1,j,k} + O(\Delta x^2),$$

where the diffusion coefficients are evaluated at the lower and upper interfaces ($i - 0.5$ and $i + 0.5$, respectively), and the spacing Δx is the local cell width. The formulae for the *y* and *z* contributions are analogously defined.

The transverse contributions at cell interfaces are approximated as the average of surrounding cell-centered transverse gradients. For simplicity we present only the transverse components in two dimensions (where the *k* index is suppressed).

$$\left.\frac{\partial T}{\partial x}\right|_{i,j\pm1/2} \approx \frac{1}{4\Delta x}\left(T_{i+1,j\pm1} - T_{i-1,j\pm1} + T_{i+1,j} - T_{i-1,j}\right) + O(\Delta x^2)$$
$$\left.\frac{\partial T}{\partial y}\right|_{i\pm1/2,j} \approx \frac{1}{4\Delta y}\left(T_{i\pm1,j+1} - T_{i\pm1,j-1} + T_{i,j+1} - T_{i,j-1}\right) + O(\Delta y^2)$$

$$\frac{\partial}{\partial x}\left(D^{21}\frac{\partial T}{\partial y}\right) \approx \frac{D^{21}_{i+\frac{1}{2},j}}{\Delta x}\left.\frac{\partial T}{\partial y}\right|_{i+\frac{1}{2},j} - \frac{D^{21}_{i-\frac{1}{2},j}}{\Delta x}\left.\frac{\partial T}{\partial y}\right|_{i-\frac{1}{2},j} + O(\Delta x^2)$$
$$\frac{\partial}{\partial y}\left(D^{12}\frac{\partial T}{\partial y}\right) \approx \frac{D^{12}_{i,j+\frac{1}{2}}}{\Delta y}\left.\frac{\partial T}{\partial x}\right|_{i,j+\frac{1}{2}} - \frac{D^{12}_{i,j-\frac{1}{2}}}{\Delta y}\left.\frac{\partial T}{\partial x}\right|_{i,j-\frac{1}{2}} + O(\Delta y^2)$$

In two dimensions, this results in a 9-point stencil using local cells in the logical domain $[i-1, i+1] \times [j-1, j+1]$, with truncation error $O(\Delta x^2, \Delta y^2)$. In three dimensions the four additional transverse components are defined analogously, which extends the discretization to a 27-point stencil. The provided discretization is the same as that of [10].

Multigrid The advancement of the temperature field in time requires the solution of a spatially-coupled system of equations. To this end, we have chosen to use the multigrid Full Approximation Scheme [11] for the inversion of this system. The remainder of this work builds upon our previously implemented version used for solving Poisson's equation for self-gravitating mass distributions.

While presenting an in-depth review of multigrid methods is outside the scope of this report, we should note some specific aspects. First, multigrid methods are based on the idea of approximating the solution of the problem on a hierarchy of nested grids. This enables increased convergence rates due to filtering of low and high order spectral modes in the error. Information is transferred between the grids by use of restriction and prolongation operators (not discussed here). On each grid, or "level," the solution of the diffusion equation is approximated by used of a "level solver". The order in which levels are visited is defined by the cycle type; our implementation uses only the V-cycle, but other options such as W- and F-cycles could be incorporated.

Level solvers One of the most important aspects of a multigrid scheme is the level solver, which is responsible for smoothing the error on each grid in the hierarchy. Traditional isotropic level solvers utilize either Jacobi iteration, Symmetric Gauss-Seidel, or Red-Black Gauss-Seidel. For anisotropic problems these methods fail to adequately reduce error in the solution; as the amount of anisotropy increases, it becomes increasingly difficult to damp error in the weakest direction [12].

Consequently, level solvers for anisotropic problems attempt to treat the smoothing operation in a directionally-split manner to damp error in both the strong and weak directions. One popular technique is to perform line or plane relaxation (in 2D and 3D, respectively). In line relaxation, one sweeps through the two-dimensional plane and updates unknowns on a chosen coordinate line simultaneously. For example, in *y-line relaxation*, each *x*-coordinate is visited in sequence and all unknowns in the *y* extent are updated simultaneously. For plane relaxation in three-dimensions, solutions are simultaneously updated on planes instead of lines.

Alternating Zebra Gauss-Seidel We have chosen to use the Alternating Zebra Gauss-Seidel (AZGS) method [13], which is a robust line/plane solver. For two-dimensional problems, AZGS is composed of two stages: a horizontal line relaxation followed by a vertical line relaxation. For a grid of size $n_I \times n_J$, a single application of horizontal line relaxation is described by the procedure:

- for all $j \in [1, n_J]$ odd, $1 \leq i \leq n_I$, solve

$$[A^{\nu}_{i-1,j} \quad A^{\nu}_{i,j} \quad A^{\nu}_{i+1,j}]T^{\nu+1}_{i,j} + \begin{bmatrix} A^{\nu}_{i-1,j+1} & A^{\nu}_{i,j+1} & A^{\nu}_{i+1,j+1} \\ - & - & - \\ A^{\nu}_{i-1,j-1} & A^{\nu}_{i-1,j-1} & A^{\nu}_{i+1,j-1} \end{bmatrix} T^{\nu}_{i,j} = f^{\nu-1}_{i,j} + f^{\nu}_{i,j}$$

- for all $j \in [1, n_J]$ even, $1 \leq i \leq n_I$, solve

$$[A^{\nu}_{i-1,j} \quad A^{\nu}_{i,j} \quad A^{\nu}_{i+1,j}]T^{\nu+1}_{i,j} + \begin{bmatrix} A^{\nu+1}_{i-1,j+1} & A^{\nu+1}_{i,j+1} & A^{\nu+1}_{i+1,j+1} \\ - & - & - \\ A^{\nu+1}_{i-1,j-1} & A^{\nu+1}_{i-1,j-1} & A^{\nu+1}_{i+1,j-1} \end{bmatrix} T^{\nu+1}_{i,j} = f^{\nu-1}_{i,j} + f^{\nu}_{i,j}$$

where the matrix $A^{\nu}(T^{\nu})$ encapsulates the spatio-temporal discretization of the diffusion operator acting on T, $f^{\nu}(T^{\nu})$ is the temporal discretization of the source term S, and ν is a fiducial representation of the current multigrid iterate. The process for vertical line relaxation is analogously defined, solving for the unknown values of T along the j indices.

The procedure above describes a set of n_J quasi-independent tridiagonal systems, each of which can be approximately or exactly solved. While each line relaxation is expected

to perform well when there is strong coupling along their individual directions, their combination through AZGS allows relaxing problems with arbitrarily oriented anisotropies.

Implementation comments for block-AMR grids The theoretical framework for multigrid with line-based relaxations becomes muddled when extended to practical problems involving parallelized, block-AMR grids. In particular, we note 1) the data required for a line relaxation across the computational domain is distributed in processor space, and 2) the concept of coarsening and refinement is no longer applied uniformly throughout the computational domain.

The first concern is resolved by communicating ghost cell information between blocks after each sweep of the AZGS procedure on the current level. Once this is communicated, the first two interior layers of zones in the block are relaxed with a local Gauss-Seidel smoothing step. This serves to couple the information from adjacent blocks without requiring additional applications of AZGS.

The second issue requires careful treatment. In particular, the restriction/prolongation operations required to properly set ghost cell data are already complicated for isotropic diffusion problems. The addition of the 9-point stencil in our spatial discretization not only requires that the ghost cells lying on a face of the block be updated, but also that the ghost cells at the corners of the block be as well. Implementation of the required communication patterns and operators in an ongoing portion of this work. Therefore, in the following verification tests we will use uniformly refined block-AMR grids with 8x8 zones per block.

Verification We are interested in anisotropic systems for which the elements of the diffusion tensor $\boldsymbol{D}$ are represented (in two dimensions) as

$$\begin{aligned} D_{11} &= \kappa_{\parallel} b_x^2 + \kappa_{\perp}(1 - b_x^2), \\ D_{21} &= \kappa_{\parallel} b_x b_y - \kappa_{\perp} b_x b_y - \kappa_{\wedge} b_z, \\ D_{22} &= \kappa_{\parallel} b_y^2 + \kappa_{\perp}\left(1 - b_y^2\right), \\ D_{12} &= \kappa_{\parallel} b_x b_y - \kappa_{\perp} b_x b_y + \kappa_{\wedge} b_z, \end{aligned}$$

where b_i are the normalized components of a vector $\boldsymbol{B}(\boldsymbol{x})$, $\kappa_{\parallel}(T)$ is the transport coefficient in the direction of $\boldsymbol{B}$, while $\kappa_{\perp}(T)$ and $\kappa_{\wedge}(T)$ are the transport coefficients in the plane orthogonal to $\boldsymbol{B}$. Physically, this model corresponds to electron heat conduction confined by a magnetic field in a plasma.

Annular transport Here we demonstrate a test problem which is, physically, quite similar to the application problems we are interested in. This test case is based on that of [10] and considers transport constrained by a circular vector field inside the domain $[-1,1]^2$, with $\kappa_{\parallel} = 1$ and $\kappa_{\perp} = \kappa_{\wedge} = 0$. The components of the vector field are defined as

$$\begin{aligned} B_x(\boldsymbol{x}) &= \sin(\phi), \\ B_y(\boldsymbol{x}) &= \cos(\phi), \\ B_z(\boldsymbol{x}) &= 0, \end{aligned}$$

where $\phi = \operatorname{atan}(y/x)$. The initial scalar field is provided by

$$T_0(\boldsymbol{x}) = \begin{cases} 12, & 0.5 < |\boldsymbol{x}| < 0.7, \frac{5\pi}{12} \leq \phi \leq \frac{7\pi}{12} \\ 10, & \text{otherwise} \end{cases}.$$

The constraint of parallel transport should prohibit any transfer through the surfaces at $|\boldsymbol{x}| = 0.5$ and $|\boldsymbol{x}| = 0.7$, thus confining the temperature evolution to an annulus. However, our spatial discretization does not allow for such a curved surface which leads to a non-zero flux into grid cells outside of the annulus.

Figure 7 shows the temporal evolution of this system at $t = 0, 100,$ and 200 for Crank-Nicolson (CN) at Courant factors of 100 and 1000, and backward Euler (BE) for Courant 1000. The V-cycle multigrid process is performed with 8 pre-smoothing steps and 1 post-

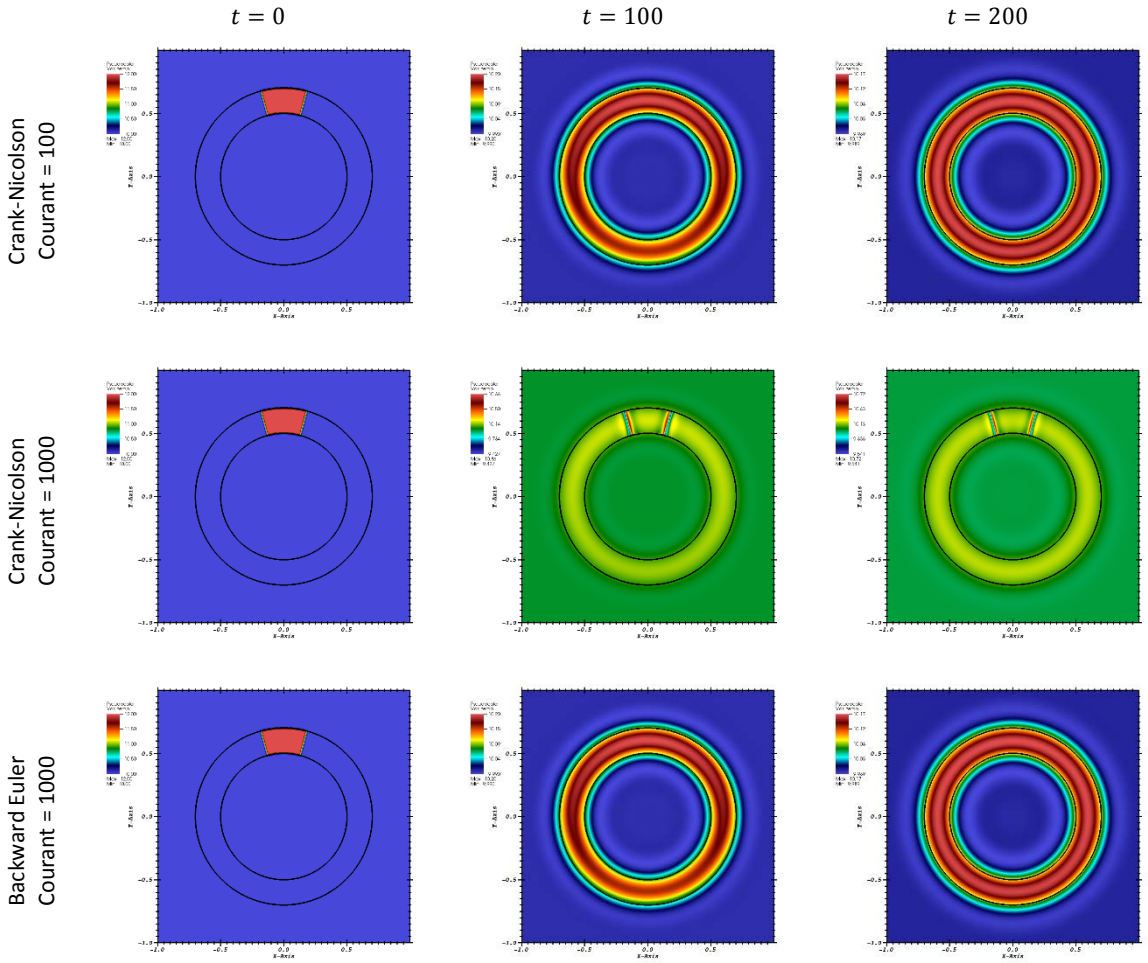

Figure 7: Evolution of temperature fields over time for multiple solvers and Courant factors. Columns denote $t = 0, 100, 200$ from left to right. (Top row) Crank-Nicolson with Courant 100. The temperature diffuses primarily along the vector field, with radial diffusion caused by the spatial discretization. (Middle row) Crank-Nicolson with Courant 1000. This scheme breaks down at large Courant factors, generating unphysical oscillations at the initial discontinuity in temperature. (Bottom row) Backward Euler with Courant 1000. This scheme can be pushed to large Courant numbers at the price of temporal accuracy.

smoothing step. Convergence of a multigrid cycle is satisfied when the norm of the residual is less than 10^{-9} of the norm of the spatiotemporal discretization of the previous timestep (the right-hand-side of the discretization equation).

For the CN at a Courant of 100, the diffusion of T is visibly transported along the circular vector field. Over time, however, evolution of the temperature field outside of the annulus is readily noticeable. For CN at Courant 1000, however, the solution becomes highly

oscillatory at the initial temperature jump. While the CN method is unconditionally stable, it is not guaranteed to be non-oscillatory. This is a result of Crank-Nicolson being the combination of a forward Euler half-step and a backward Euler-half step. Any forward Euler contribution is eliminated when $\theta = 1$, which is just the backward Euler case. The BE models at Courant 1000 evolve as expected.

While the order of the temporal truncation error differs between CN and BE, the models presented are dominated by the spatial discretization error. As models are computed with high fidelity grids, however, this error will manifest. Therefore, to maintain a formally $O(\Delta t^2)$ error at large Courant factors, and without oscillations, methods such as Richardson extrapolation can be applied, which is composed of two backward Euler half-timesteps.

Note the undershooting behavior from the numerical diffusion normal to the annulus surface. This characteristic of the central differencing scheme employed in the spatial discretization when coupled with relatively strong gradients in the solution. If this it determined to be a problem in real simulations, the problem may be mitigated by using quasi-upwinding schemes for the spatial discretization.

Grid-aligned transport Our first case considers diffusive transport in the unidirectional field $\boldsymbol{B} = \hat{\boldsymbol{x}}$, with $\kappa_{\parallel} = 1$ and $\kappa_{\perp} = \kappa_{\wedge} = 0$. The scalar field T is initialized on the periodic domain $[-1,1]^2$ such that

$$T_0(\boldsymbol{x}) = \begin{cases} 12, & |\boldsymbol{x}| < 0.5 \\ 10, & |\boldsymbol{x}| \geq 0.5 \end{cases}.$$

The V-cycle multigrid process is performed with 8 pre-smoothing steps and 1 post-smoothing step. Convergence of a multigrid cycle is satisfied when the norm of the residual is less than 10^{-9} of the norm of the spatiotemporal discretization of the previous timestep (the right-hand-side of the discretization equation).

1.4 Future work

The original (hemispherical) target design has currently little chances to be fielded on NIF because of possible damage to the optical systems due to target shrapnels. We will therefore consider a design where the target is a cone with opening angle 0<α<180°, which is in between the cylindrical tube used in the planar design (α=0°) and the hemisphere used in the original design (α=180°). In this way, one can reduce the danger due to target shrapnels while still keeping the effects due to divergence. We will perform a series of simulations with different opening angles α in order to decide which opening angle can be tolerated. Specific physics questions that will be addressed within this study are shock-proximity effects (shock deformation), inter-shell penetration via turbulent mixing and shell breakouts.

Because several basic physics and experimental components are shared between the planar RTI designs and Kelvin-Helmholtz HEDP experiments, studying the latter system in some detail using the extended Proteus code appears very interesting. As the implementation of the additional code modules is finished, we will be able to perform sensitivity analysis and subgrid-scale modeling of the Kelvin-Helmholtz instability. The envisioned parameter study involves the key parameters of interest (Mach number, Atwood number, viscosity coefficient, mixed-layer width) with reasonable ranges of values. The required computational framework then will create and execute a series of

simulation experiments based on every combination of these values in order to probe the entire parameter space of the problem. We will then able to analyze the database of the results and extract the numerical KHI growth rates. The numerical growth rates can be estimated using the kinetic energy due to the velocity component tangent to the interface, and compare to theoretical results.

3. Products

We have new experimental design to study blast-wave driven RT instability on NIF. The major paper presenting the planar target design, related simulations and analysis, was published in 2014 in High Energy Density Physics [5]. The second paper in the planar design series was published in 2015 in the same journal. In this paper we focused on the evolution and role that self-generated magnetic fields play in the planar SNRT experiments [9].

The results of our design work were presented in poster sessions at the 80th Annual Meeting of Southeastern Section of American Physical Society in Tallahassee, FL, and a contributed talk and poster at the international conference, Magnetic Fields in the Universe IV: From Laboratory and Stars to the Primordial Structures, held in Playa del Carmen, Mexico, February 4-8, 2013. A brief presentation of the planar target design study has been published in the conference series of RevMexAA. Posters of the project were presented at the NIF users group meeting 2013, the Plasma Physics Conference 2014 and the NIF users group meeting 2014.

In the course of the project, our design code, Proteus, has been significantly expanded to include additional plasma physics modules. In particular, Proteus now allows to study evolution of HEDP systems using single fluid MHD approximation (the Braginskii model) taking into account the effects of self-generation of magnetic fields, thermal and friction forces, and anisotropic viscous and plasma conductivity effects.

4. Participants and other collaborating organizations

The main contributors to the project were Dr. Markus Flaig, Dr. Timothy Handy, and doctoral candidate, Mr. Ryan Learn. Both Dr. Flaig and Dr. Handy were fully (1 FTE) supported in this project as postdoctoral research associates in Year 1-3 (Dr. Flaig) and during the no-cost extension period (Dr. Handy). No support was provided to Ryan Learn, who acted as an informal contributor.

A group of informal project participants also included long-term collaborators from the University of Michigan (Dr. P. Keiter, Prof. R. P. Drake, Dr. C. Kuranz) and LLNL (Dr. Hye-Sook Park, Dr. A. Miles, Dr. B. Remington). Dr. Hye-Sook Park was our NIF Diverging Supernova RTI Project Science Liaison. Drs. Plewa and Flaig had a status of LLNL collaborators and used computing resources of LLNL OCF systems to conduct majority of design simulations. Additional computations were performed at the University of Michigan and DOE SC NERSC supercomputer center.

References

[1] Kuranz, C. C. Drake, R. P., Grosskopf, M. J., et al. 2010, Phys. Plasmas, 17, 052709
[2] Fryxell, B., Kuranz, C. C., Drake, R. P., et al. 2010, High Energy Density Phys., 6, 162
[3] Braginskii, S.I., 1965, in: Reviews of Plasma Physics (Consultants Bureau, New York), Vol. 1, 205

[4] Modica, F., Plewa, T., & Zhiglo, A. 2013, High Energy Density Phys., 9, 767
[5] Flaig, M., Plewa, T., Keiter, P. A., et al. 2014, High Energy Density Phys., 12, 35
[6] Oron, D., Arazi, L., Kartoon, D., et al. 2001, Phys. Plasmas, 8, 2883
[7] Miles, A. R., Braun, D. G., Edwards, H. F., et al. 2004, Phys. Plasmas, 11, 3631
[8] Kifonidis, K., Plewa, T., Scheck, L., et al. 2006, Astron. Astrophys., 453, 661
[9] Flaig, M., & Plewa, T. 2015, High Energy Density Phys., 17, 46
[10] Parrish, I. J., & Stone, J. M. 2005, Astrophys. J., 633, 334
[11] Brandt, A. 1984, Multi-grid techniques: 1984 guide with applications to fluid dynamics. GMD-Studien. no 85 (St. Augustin, Germany)
[12] Briggs, W., Henson, V. E., & McCormick, S. F. 2000, A multigrid tutorial, 2nd edition (SIAM: Philadelphia)
[13] Wesseling, P. 1992, An introduction to multigrid methods, (Wiley: New York)